

## A 2-Site Model for Simulating Supercritical Fluoroform

W. Song, N. Patel, and M. Maroncelli\*

Department of Chemistry, The Pennsylvania State University, University Park, Pennsylvania 16802

Received: April 29, 2002; In Final Form: June 28, 2002

A 2-site model of fluoroform ( $\text{CHF}_3$ ) has been developed for use in simulations of solvation in the near critical regime. The model was optimized to reproduce the critical point and the liquid–vapor coexistence curve of the real fluid using the Gibbs Ensemble Monte Carlo method. Additional Monte Carlo and molecular dynamics simulations demonstrate that this simplified model also reproduces a number of other properties of  $\text{CHF}_3$  relevant to its use in simulations of solvation and reaction. Along a near critical isotherm, vapor pressures, dielectric constants, self-diffusion coefficients, and viscosities are all found to be within 15% of experimental values. The main shortcoming of the model appears to be in its representation of the rotational dynamics of  $\text{CHF}_3$  molecules, which are faster in the model compared to the real fluid by  $\sim 25\%$  at near and above the critical density.

### Introduction

Increasing use of supercritical solvents in a wide range of practical applications<sup>1</sup> has motivated numerous recent studies aimed at understanding the fundamental aspects of solvation and solvent effects on chemical reactions in such media.<sup>2–6</sup> Computer simulations, using both idealized model systems<sup>7–14</sup> as well as fairly realistic solute and solvent representations,<sup>15–19</sup> have played a particularly valuable role in these efforts. Research in our group has focused on attempts to model experimental results on solvatochromic shifts and simple solute dynamics in near-room-temperature supercritical solvents.<sup>18–21</sup> Our work to date has considered only simulations of nonpolar (ethane) or nondipolar ( $\text{CO}_2$ ) supercritical solvents using models developed by others.<sup>22,23</sup> To extend this work to a dipolar supercritical fluid, we have developed a simplified but accurate model of supercritical fluoroform, whose parametrization and performance are the subject of the present paper.

Fluoroform ( $\text{CHF}_3$ ) possesses a significant dipole moment ( $1.65 \text{ D}^{24}$ ), has a conveniently located critical point ( $T_c = 26.1^\circ\text{C}$ ,  $P_c = 48 \text{ bar}^{25}$ ), is nontoxic and is relatively benign to the environment, and is available in high purity at modest cost. For these reasons, fluoroform has served as the prototype for polar supercritical solvents in numerous experimental studies over the past decade.<sup>26–38</sup> Several simulation models of fluoroform have already been developed<sup>39–45</sup> and successfully applied to study a number of properties of the neat fluid.<sup>38</sup> However, to our knowledge these models have yet to be applied to studies of solvation phenomena, i.e., to studies beyond those of neat fluid. One reason may be the computational expense of these models, nearly all of which use “all-atom” representations having five interaction sites per molecule.<sup>46</sup> Although such models are expected to be more realistic than reduced representations, the amount of computation involved is a disadvantage for studies of solvation phenomena in the compressible regime, where large numbers of solvent molecules and long trajectories are typically required for adequate sampling. For this reason, we decided to seek a simplified model of fluoroform—one that would be less expensive than the all-atom versions but which would still

reproduce most of the properties of the experimental fluid with reasonable accuracy. Using the Gibbs ensemble Monte Carlo method<sup>47</sup> we have parametrized a 2-site model to best reproduce the experimental liquid–vapor coexistence curve and critical point of fluoroform. Isothermal simulations as a function of density above the critical point show that this model yields surprisingly accurate results for a number of static as well as dynamical properties of the neat fluid. This accuracy, coupled to its economy (a factor of 4/25 in calculating intermolecular pair interactions) should render the model useful in future studies of supercritical solvation.

### Potential Model and Simulation Details

To represent  $\text{CHF}_3$  molecules we use a pair of sites separated by a distance  $d$  as origins of pairwise Lennard-Jones and Coulomb interactions between molecules. We initially considered models in which the Lennard-Jones parameters of the two sites were distinct. We found, however, that a model in which the two interaction sites are identical except for charge is sufficient to reproduce the coexistence behavior. The interaction between two molecules  $i$  and  $j$  is thus of the form

$$u_{ij} = \sum_{i_a=1}^2 \sum_{j_b=1}^2 \left\{ \frac{q_{i_a} q_{j_b}}{r_{i_a j_b}} + 4\epsilon \left[ \left( \frac{\sigma}{r_{i_a j_b}} \right)^{12} - \left( \frac{\sigma}{r_{i_a j_b}} \right)^6 \right] \right\} \quad (1)$$

where  $r_{i_a j_b}$  is the distance between site  $a$  on molecule  $i$  and site  $b$  on molecule  $j$ , and  $q_{i_a}$  is the charge on site  $i_a$ . Our approach to determining the parameters in the model is as follows.

The site masses ( $m$ ) and separation ( $d$ ) were chosen to reproduce the total mass ( $70.02 \text{ amu}$ ) and rotational constant ( $10348.867 \text{ GHz}^{24}$ ) of the  $\text{CHF}_3$  molecule. The charges  $q$  were chosen to provide a dipole moment  $\sim 25\%$  larger than that of the gas-phase molecule ( $1.646 \text{ D}^{24}$ ) in order to approximate the effect of induced charges in the dense fluid. The charge was fine-tuned in order to reproduce the dielectric constant of the real fluid at twice the critical density and a temperature of  $310 \text{ K}$ .

The Lennard-Jones parameters  $\epsilon$  and  $\sigma$  were then varied in order to optimize agreement with the vapor–liquid coexistence

\* Corresponding author.

properties. As a starting point, we first varied the parameters so as to reproduce (appropriately scaled<sup>48</sup>) experimental values of the second pressure virial coefficients. (See the discussion surrounding Figure 3 for more details.) The parameters so obtained were then used in Gibbs Ensemble Monte Carlo (GEMC) simulations and further tuned to reproduce experimental values of the coexisting liquid and vapor densities and the location of the critical point. The critical temperature  $T_c$  and critical density  $\rho_c$  were extrapolated from coexistence data by fitting them to the relations<sup>49</sup>

$$\frac{1}{2}(\rho_L + \rho_V) \cong \rho_c + A(T - T_c) \quad (2)$$

$$\rho_L - \rho_V \cong B(T - T_c)^\beta \quad (3)$$

where  $\rho_L$  and  $\rho_V$  are the coexisting liquid and vapor densities and  $A$  and  $B$  are adjustable parameters. The critical exponent  $\beta$  was given a value of  $1/3$  in these fits, rather than the theoretical value of  $0.32$ ,<sup>49</sup> since the former value provided better predictions of the experimental critical parameters when using a comparable set of experimental data. The results were then compared to the experimental critical parameters, the Lennard-Jones parameters appropriately adjusted, and the process repeated until satisfactory agreement between the calculated and experimental values was achieved.

Three types of simulations were performed in this work: GEMC simulations of the liquid–vapor phase coexistence, as well as standard Monte Carlo (MC) and molecular dynamics (MD) simulations, which were used to calculate other static and dynamic properties of interest. In all cases cubic periodic boundary conditions were applied and long-range interactions treated using a 10th order Kubic harmonic approximation to the Ewald sum.<sup>50</sup>

Our implementation of the GEMC method is essentially as described in Frenkel and Smit.<sup>49</sup> Simulations were performed with a total of  $N_{\text{mols}} = 686$  or 637 molecules distributed between high and low density boxes. At temperatures below 250 K, the simulation was initialized with 125 molecules at a vaporlike density in one box and 512 molecules at a liquidlike density in the other. At higher temperatures, the two boxes were started at the same average density within the unstable region, with 343 molecules in each box. A Monte Carlo step in these simulations consisted of attempting one of three kinds of moves: a translational or rotational displacement with probability  $N_{\text{mols}}/N_{\text{tot}}$ , a volume exchange with probability  $N_{\text{vol}}/N_{\text{tot}}$ , or an exchange of molecules between boxes with probability  $N_{\text{swap}}/N_{\text{tot}}$ , where  $N_{\text{tot}} = N_{\text{mols}} + N_{\text{vol}} + N_{\text{swap}}$ . Good results were obtained with  $N_{\text{vol}} = 1$  and  $N_{\text{swap}}$  varied between 3000 at 220 K and 50 at 290 K. Step sizes were chosen to provide acceptance ratios of 40–60% for both translation–rotation and volume exchange, whereas the acceptance ratios for molecule exchange were between 1 and 4%. A GEMC simulation for a particular temperature typically consisted of  $3 \times 10^6$  steps of equilibration starting from a lattice configuration, followed by  $6 \times 10^6$  steps of data collection. Canonical MC simulations were similar to the GEMC simulations except for the use of a single box and the absence of particle exchange. All of the latter simulations were performed with a total of 343 molecules. The Lennard-Jones potentials for both the canonical MC and the GEMC simulations were truncated at an intermolecular separation equal to half of the box length, and long-range tail corrections applied.

Molecular dynamics simulations were performed with 864 molecules using the leapfrog algorithm for linear molecules

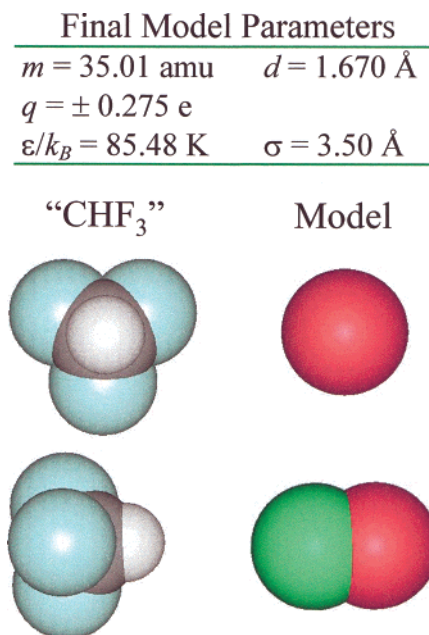


**Figure 1.** Final model parameters and schematic comparison of the size and shape of a CHF<sub>3</sub> molecule and the 2-site model developed here.<sup>67</sup>

proposed by Fincham<sup>51</sup> with a time step of 2 fs. For each density, a constant-NVT simulation was run for 1 ns, starting from a lattice configuration to equilibrate the system, and then a 2 ns NVE run was performed during which time data was collected for later analysis.

### Performance of the Model

Optimized parameters of the model potential are listed in Figure 1 together with a schematic comparison of the size and shape of CHF<sub>3</sub> and the 2-site representation adopted here. The purpose of this comparison is to highlight the fact that this model grossly distorts the actual shape of a CHF<sub>3</sub> molecule. The molecular volume<sup>52</sup> of the model diatomic is similar to that of the real molecule, but is smaller by roughly 9%. Despite these steric differences, the model is able to accurately reproduce many of the static and dynamic features of the real fluid.

The primary data used for fitting the potential were the coexisting liquid and vapor densities at a series of 10 temperatures between 220 K and 290 K (Table 1). Figure 2 shows the experimental coexistence data<sup>25</sup> (solid curves) along with densities obtained from GEMC simulations (circles). As illustrated in this figure, the model provides an excellent fit of the experimental coexistence data. The critical temperature is estimated to be  $300.2 \pm 1.4 \text{ K}$ , in agreement with the experimental value of  $299.3 \text{ K}$ .<sup>25</sup> The calculated critical density,  $0.541 \pm 0.006 \text{ g/cm}^3$ , is slightly higher than the experimental value of  $0.526 \text{ g/cm}^3$ ,<sup>25</sup> as are the liquid-phase densities, with the difference ranging from 1% at lower temperatures to 3% near the critical point.

Other indicators of the ability of the model to reproduce static properties of CHF<sub>3</sub> are provided in Figures 3–5. (Data presented in these and the following figures are also tabulated in the Supporting Information). Figure 3 illustrates the low-density behavior of the model via a comparison of observed<sup>53</sup> (points) and calculated (curves) values of the second pressure virial coefficients,  $B_2(T)$ . The solid curve is calculated directly from the model potential. Since this model is parametrized to reproduce the high density behavior of fluorine using (fixed) effective parameters, it deviates systematically from these low-

TABLE 1: Simulated Properties along the Coexistence Curve<sup>a</sup>

N	T/K	liquid phase			vapor phase			$\Delta H^{\text{vap}}/\text{kJ mol}^{-1}$
		$P_L/\text{MPa}$	$\rho_L/\text{g cm}^{-3}$	$U_L/\text{kJ mol}^{-1}$	$P_V/\text{MPa}$	$\rho_V/\text{g cm}^{-3}$	$U_V/\text{kJ mol}^{-1}$	
686	290	3.65 (14)	0.875 (23)	-8.62 (16)	3.76 (14)	0.253 (22)	-4.01 (29)	5.35 (47)
	285	3.38 (27)	0.951 (17)	-9.13 (12)	3.19 (9)	0.176 (13)	-2.88 (20)	7.27 (17)
	280	2.79 (25)	0.996 (7)	-9.52 (4)	2.84 (11)	0.148 (6)	-2.60 (9)	8.42 (16)
	275	3.15 (39)	1.051 (7)	-9.94 (6)	2.68 (8)	0.137 (5)	-2.38 (8)	8.75 (9)
	270	2.37 (64)	1.085 (9)	-10.27 (8)	2.26 (7)	0.106 (4)	-1.94 (6)	9.67 (13)
	260	1.75 (66)	1.146 (7)	-10.83 (7)	1.75 (7)	0.079 (2)	-1.58 (3)	10.69 (17)
	250	1.82 (77)	1.200 (11)	-11.36 (10)	1.23 (4)	0.055 (1)	-1.17 (6)	11.63(10)
637	240	1.31 (85)	1.252 (8)	-11.86 (8)	0.92 (1)	0.041 (1)	-1.05 (3)	12.30(8)
	230	1.32 (30)	1.312 (4)	-12.50 (5)	0.60 (1)	0.027 (1)	-0.77 (4)	12.98(13)
	220	0.68 (17)	1.350 (7)	-12.84 (8)	0.49 (1)	0.022 (1)	-0.73 (7)	13.52(11)

<sup>a</sup> N is the total number of molecules in the simulation,  $P_X$  the average pressure,  $\rho_X$  the average density, and  $U_X$  the average configurational energy of phase X.  $\Delta H^{\text{vap}}$  is the enthalpy of vaporization calculated according to eq 4. Values in parentheses are 95% confidence limits based on statistical variations in 10 sub-averages.

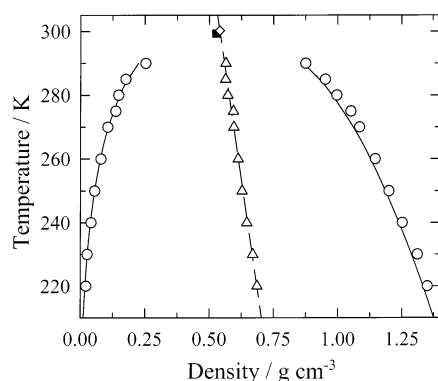


**Figure 2.** Coexisting liquid and vapor densities of  $\text{CHF}_3$  over the temperature range 220–290 K. Open circles denote simulated data and solid circles represent parametrizations of experimental data.<sup>25</sup> The triangular points are the “rectilinear diameters”  $(1/2)(\rho_L + \rho_V)$  and the dashed line the fit to these diameters used to determine the critical point of the model (eq 2). The open diamond and filled square, respectively, mark the simulated  $(0.541 \pm 0.006 \text{ g/cm}^3, 300.2 \pm 1.4 \text{ K})$  and experimental  $(0.526 \text{ g/cm}^3, 299.3 \text{ K})$  critical points.

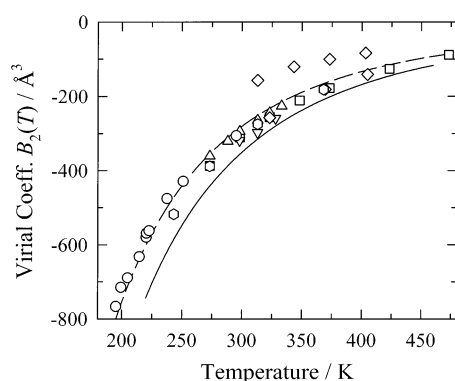


**Figure 3.** Temperature dependence of the second pressure virial coefficient  $B_2(T)$  of  $\text{CHF}_3$ . Symbols denote experimental data from the compilation of Dymond and Smith,<sup>53</sup> with different symbols used for data from different laboratories. The solid curve is the  $B_2(T)$  dependence calculated directly from the model pair potential and the dashed curve shows the former result scaled according to  $B_2(0.91T)$ .

density data. However a scaling of the temperatures of the calculated  $B_2(T)$  data by a factor of 0.91 (dashed curve) brings about agreement with the experimental data, at least to within the substantial variability of data from different sources. This observation is in keeping with the behavior we have noted for other effective pair potentials that are tuned to simulate fluids in the vicinity of the critical point.<sup>20</sup> In the present case, the effective pair potential reproduces the dense fluid properties by

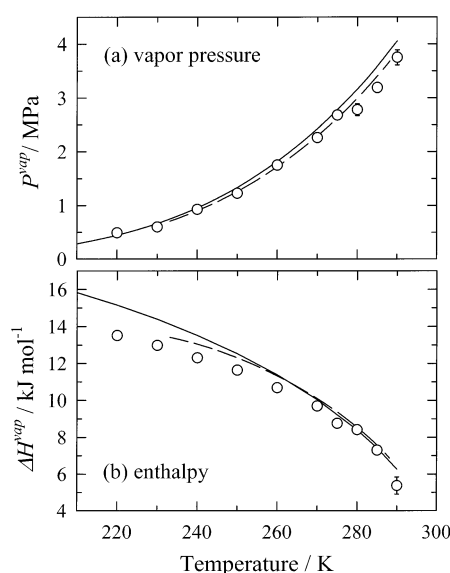


**Figure 4.** (a) Vapor pressures and (b) enthalpies of vaporization of  $\text{CHF}_3$  along the saturation curve. Circles denote simulated data and the solid and dashed curves denote parametrizations of experimental data by Rubio et al.<sup>54</sup> and Altunin et al.<sup>55</sup> respectively.

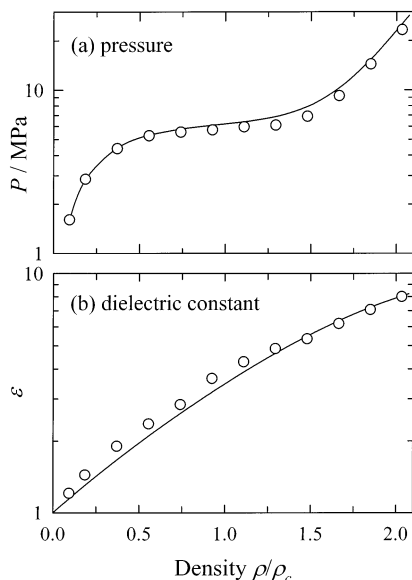
increasing the net attraction between two molecules by about 9% relative to the true pair potential.

Figure 4 compares simulated and experimental results for the vapor pressures  $P^{\text{vap}}$  and enthalpies of vaporization  $\Delta H^{\text{vap}}$  along the coexistence curve. Two different parametrizations of experimental data are represented here by solid<sup>54</sup> and dashed lines.<sup>55</sup> The simulated vapor pressures (Figure 4a) agree with the parametrization of Altunin et al.<sup>55</sup> to within simulation uncertainties (approximately the size of the points) and are systematically lower than those of Rubio et al.<sup>54</sup> by  $\sim 6\%$ . Extrapolation of the linear behavior of  $\ln P^{\text{vap}}$  vs  $T^{-1}$  to the critical point of the model yields a critical pressure of  $4.6 \pm 0.2 \text{ MPa}$ , in agreement with the experimental value of  $4.84 \text{ MPa}$ .<sup>25</sup>

Enthalpies of vaporization (Figure 4b) were calculated from the equation

$$\Delta H^{\text{vap}} = U_V - U_L + P^{\text{vap}} (\rho_V^{-1} - \rho_L^{-1}) \quad (4)$$

where  $U_V$  and  $U_L$  are the configuration energies of the vapor and liquid, respectively. In this case the simulated results are slightly smaller than both sets of parametrized experimental data, by an average of 7% (Rubio et al.<sup>54</sup>) and 5% (Altunin et al.<sup>55</sup>).



**Figure 5.** (a) Pressures and (b) dielectric constants of  $\text{CHF}_3$  as a function of density at 310 K. Simulated results are shown as circles (uncertainties smaller than the symbols) and parametrizations of experimental data as solid curves.<sup>54,56</sup> Note the logarithmic scale used for the ordinates in these plots.

Thus, the cohesive energy of the liquid, especially at lower temperatures, appears to be slightly underestimated by the model.

Of most interest for our own purposes is the accuracy with which the model can reproduce the density dependence of properties above, but near to, the critical temperature. To examine this regime, additional MC simulations were carried out on the supercritical isotherm at 310 K ( $T/T_c = 1.03$ ) as a function of density. Figure 5a compares the pressures simulated (points) on this isotherm to those obtained from the equation of state of Rubio et al.<sup>54</sup> The simulated pressures are systematically lower than the experimental pressures, but only by an average of <5% for this isotherm.

Figure 5b compares parametrized values of the measured dielectric constant of  $\text{CHF}_3$ <sup>56</sup> (solid curve) to simulated values (points), calculated according to<sup>57</sup>

$$\epsilon = 1 + \frac{4\pi\langle|\vec{M}|^2\rangle}{3k_B T V} \quad (5)$$

where  $\vec{M}$  is the total dipole moment of the system,  $\vec{M} = \sum_i \vec{\mu}_i$ ,  $k_B$  is the Boltzmann constant,  $T$  the temperature, and  $V$  the volume of the system. As pointed out in the previous section,  $q$  was chosen to reproduce the dielectric constant on this isotherm at high density. The dipole moment of the diatomic model produced in this way is 2.20 D, 33% higher than the gas-phase moment (1.648 D<sup>24</sup>) of  $\text{CHF}_3$ , as required to account for the induced component of the dipole at high densities. Using such an effective dipole moment in this nonpolarizable model yields dielectric constants that are systematically ~10% higher than the experimental values in the intermediate density region,  $0.3 < \rho/\rho_c < 1.1$ . We note that electrical solvation energies simulated with this model will likely be overestimated by more than 10%. For example, the reaction field factor related to dipole solvation,  $(\epsilon - 1)/(\epsilon + 2)$ , is overestimated by as much as 20–30% at densities below  $0.5 \rho_c$ . Inclusion of explicit polarizability or density-dependent charges is required to better reproduce the dielectric properties over the entire density range spanned here.

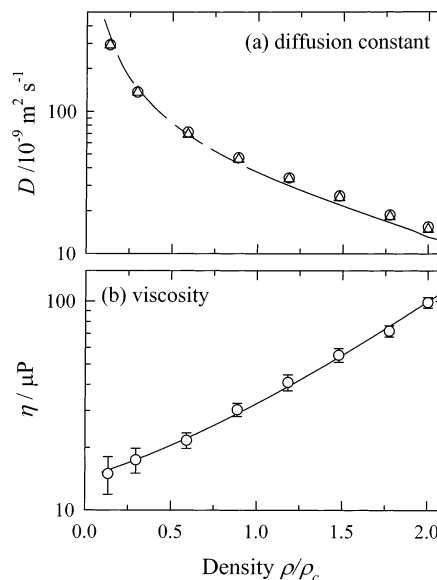


**Figure 6.** (a) Self-diffusion coefficients and (b) shear viscosities of  $\text{CHF}_3$  at 310 K. In panel (a) simulated results using both the integration of the velocity autocorrelation functions (circles) and mean square displacements (triangles) are shown. The solid line is a parametrization of the experimental data of Lang et al.<sup>58,52</sup> (see text). The dashed portion of this curve denotes extrapolation beyond the limits of the experimental data. In panel (b) the simulated results (circles) are compared to the empirical viscosity equation of Shan et al.<sup>60</sup> Note the logarithmic scale used for the ordinates in these plots.

We also examined dynamical predictions of the model on the 310 K isotherm, using data from a series of molecular dynamics simulations. Figure 6 shows results for two transport properties, the self-diffusion coefficient ( $D$ ) and the shear viscosity ( $\eta$ ). The self-diffusion coefficient was determined using the expressions

$$D = \frac{1}{3} \int_0^\infty dt \langle \vec{v}_i(t) \cdot \vec{v}_i(0) \rangle = \lim_{t \rightarrow \infty} \frac{\langle |\vec{r}_i(t) - \vec{r}_i(0)|^2 \rangle}{6t} \quad (6)$$

where  $\vec{r}_i(t)$  and  $\vec{v}_i(t)$  are the position and velocity of the center of mass of a molecule at time  $t$ .<sup>51</sup> Experimental diffusion coefficients are represented by the curve in Figure 6a. This curve was generated by fitting the data of Lang et al.<sup>58</sup> (250–383 K) using a semiempirical model of diffusion.<sup>59,52</sup> The dashed portion of this curve denotes extrapolation beyond the density range of the experimental data, and this region should therefore be viewed with skepticism. The two sets of nearly superimposed points in Figure 6a represent the two methods of calculating  $D$  expressed by eq 6, which yield very similar results. Agreement between the simulated and experimental data is better than 15% in all cases (not much larger than the anticipated uncertainties in the experimental data) with the model tending to overestimate the diffusion constant at higher densities.

Viscosities are compared in Figure 6b. The model results (points) were calculated from the Green-Kubo relation

$$\eta = \frac{V}{k_B T} \int_0^\infty dt \langle P_{\alpha\beta}(t) \cdot P_{\alpha\beta}(0) \rangle \quad (7)$$

where  $P_{\alpha\beta}$  is an off-diagonal element of the pressure tensor.<sup>51</sup> The experimental data (solid curve) are from the parametrization of Shan et al.<sup>60</sup> As can be seen from this figure, the model represents the viscosity of  $\text{CHF}_3$  to within the simulated uncertainties.



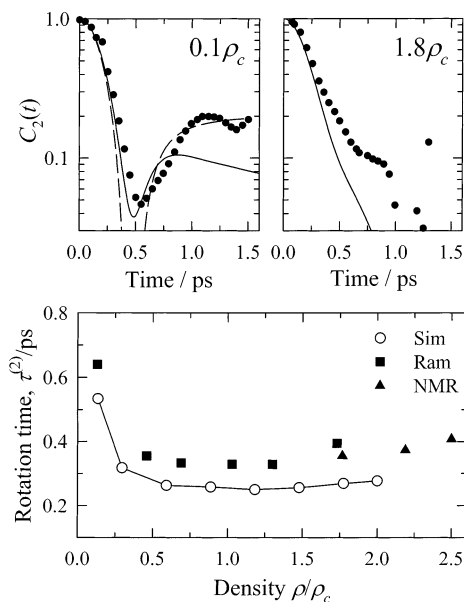


**Figure 7.** Calculated rotational autocorrelation functions ( $C_2(t)$ ; eq 8) and correlation times ( $\tau^{(2)}$ ; eq 9) of supercritical  $\text{CHF}_3$ . The top panels show correlation functions at low ( $0.13\rho_c$ ) and high densities ( $1.8\rho_c$ ). The solid curves are simulated results and the points the experimental data of Okazaki et al.<sup>37</sup> For reference, the free rotor result is also shown in the left panel (dashed curve). The bottom panel compares correlation times from simulation (connected open circles) to times deduced from Raman<sup>37</sup> (filled squares) and NMR<sup>58</sup> (filled triangles) data. (Uncertainties in the simulated times are smaller than the symbol size.) The experimental data in this figure were obtained at a temperature of 305 K, whereas the simulations were performed at 310 K; however, no significant effect of such a temperature difference is expected.

Finally, in Figures 7 and 8, we consider observables related to the rotational dynamics of  $\text{CHF}_3$  molecules. In Figure 7 we compare the single-particle orientational correlation functions

$$C_2(t) = \langle P_2[\hat{u}(0) \cdot \hat{u}(t)] \rangle \quad P_2(x) = \frac{3}{2}x^2 - \frac{1}{2} \quad (8)$$

and correlation times

$$\tau^{(2)} = \int_0^\infty C_2(t) dt \quad (9)$$

to results from Raman line shape analysis of the C–H stretch of  $\text{CHF}_3$ <sup>38</sup> and from deuterium spin–lattice relaxation measurements in  $\text{CDF}_3$ .<sup>58</sup> The top panels in Figure 7 show simulated (solid curves) and experimental<sup>38</sup> (points) correlation functions under low- and high-density conditions. For reference, the free rotor correlation function (dashed curve) is also depicted in the left-hand panel. Since the initial dynamics of  $C_2(t)$  are dominated by the inertial characteristics of individual molecules, of all of these functions decay similarly at early times, and the experiments and simulations agree to within the anticipated uncertainties in the experimental curves. At later times the simulated curves tend to fall below the experimental data at all densities studied. The correlation times in the bottom panel of Figure 7 show that the simulated rotation times are  $\sim 25\%$  smaller than the experimental times at densities approaching  $2\rho_c$ . These results imply that the friction on rotational motion is underestimated by the diatomic model—a result that would be expected on the basis of the different shapes of the model and  $\text{CHF}_3$ . (We note, for example, that the volume swept out upon rotation of the symmetry axis of  $\text{CHF}_3$  is  $\sim 25\%$  greater than the volume swept out by rotation of the diatomic model.)

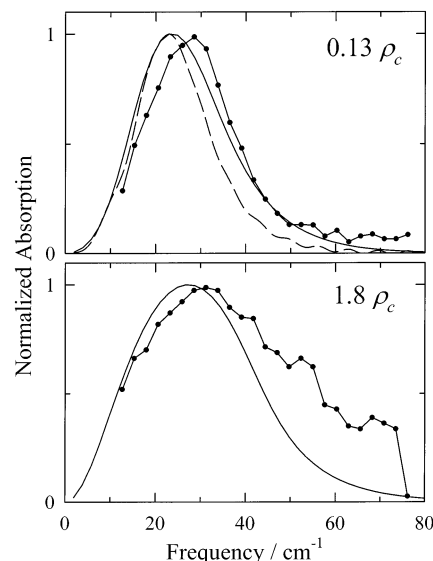


**Figure 8.** Calculated (solid curves; 310 K) and observed (connected points; 305 K) far-infrared spectra of  $\text{CHF}_3$  at two densities. The experimental data are from the THz experiments of Saitow et al.<sup>34</sup> The dashed curve in the top panel is the free rotor result.

The collective reorientational dynamics contained in the system dipole moment correlation function,

$$C_M(t) = \frac{\langle \vec{M}(0) \cdot \vec{M}(t) \rangle}{\langle |\vec{M}|^2 \rangle} \quad (10)$$

are reflected in the far-infrared (FIR) absorption spectra displayed in Figure 8. The experimental data here (connected points) are from the THz experiments of Saitow et al.<sup>34</sup> Simulated absorption spectra,  $\alpha(\omega)$ , were generated from  $C_M(t)$  according to the relations,<sup>61,62</sup>

$$\alpha(\omega) = \frac{\omega}{c} \frac{\epsilon'(\omega)}{n(\omega)} \quad (11)$$

where

$$\epsilon'(\omega) = \epsilon_\infty + (\epsilon_0 - \epsilon_\infty)[1 - \omega \int_0^\infty \sin(\omega t) C_M(t) dt] \quad (12a)$$

$$\epsilon''(\omega) = (\epsilon_0 - \epsilon_\infty) \omega \int_0^\infty \cos(\omega t) C_M(t) dt \quad (12b)$$

$$n^2(\omega) = \frac{1}{2}[\epsilon'(\omega) + \sqrt{\epsilon'(\omega)^2 + \epsilon''(\omega)^2}] \quad (13)$$

and  $c$  is the speed of light.<sup>63</sup> Comparing the calculated and observed spectra one finds that there is moderately good agreement of the peak position and location of the low-frequency edge of the spectrum, however, at all but the lowest densities, the extent of the high-frequency wing of the spectrum is significantly underestimated by the simulations. It seems likely that this shortcoming again reflects inaccuracies in the representation of rotational friction, here manifest as less prominent librational components in the spectrum. The difference may also be reasonably attributed to the smaller rotational volume of the diatomic model compared to  $\text{CHF}_3$ .

## Summary and Conclusions

We have developed a 2-site model of  $\text{CHF}_3$  for use in simulations of supercritical solvation. The model parameters were optimized to fit to the experimental vapor–liquid coexist-

ence curve and dielectric constant at high density. The critical point estimated for the model is  $(0.541 \pm 0.006 \text{ g/cm}^3, 300.2 \pm 1.4 \text{ K})$ , very close to that of the real fluid  $(0.526 \text{ g/cm}^3, 299.3 \text{ K})$ . Over the range 220–285 K, experimental vapor pressures and enthalpies of vaporization at coexistence are reproduced to within 10%. Along the single supercritical isotherm studied (310 K) a variety of other static and dynamic properties of  $\text{CHF}_3$  were also found to be reproduced with reasonable accuracy over the entire density range  $0-2\rho_c$ , i.e., vapor pressures (<5%), dielectric constants (<15%), self-diffusion constants (<15%), and viscosities (within uncertainties). These results suggest that simulations employing this model solvent should be realistic enough to enable direct comparison to experimental data on solvation in supercritical  $\text{CHF}_3$ . Its simplicity makes it especially attractive in this context by virtue of the greatly reduced computational effort required for simulating 2-site versus all-atom models.

There are, of course, some drawbacks to this simplified representation that should be kept in mind. First, we note that the rotational dynamics of the model are faster than those of the real fluid (by 25% based on  $\tau^{(2)}$  data) and thus time-dependent solvation properties, at least those emphasizing solvent reorientational dynamics, should also be too fast compared to experiment. In addition, the use of fixed solute charges, determined to reproduce the high-density dielectric constant of the real fluid, will overestimate electrical solvation energetics at low densities and distort the density dependence of these energies. The same error would be made by all-atom models unless density-dependent parameters<sup>64</sup> or (preferably) explicit polarizabilities<sup>39</sup> are used. The 2-site model could be readily extended to include polarizability at reasonable computational cost, and we will consider such an extension in future work.

**Acknowledgment.** This work was supported by a grant from the National Science Foundation (CHE-9980383) and a fellowship from the John Simon Guggenheim Memorial Foundation.

**Supporting Information Available:** Three tables: pressures and dielectric constants at 310 K, self-diffusion coefficients and viscosities at 310 K, and rotation times. This material is available free of charge via the Internet at <http://pubs.acs.org>.

## References and Notes

- (1) *Chemical Synthesis using Supercritical Fluids*; Jessop, P. G., Leitner, W., Eds.; Wiley-VCH: New York, 1999.
- (2) Kajimoto, O. *Chem. Rev.* **1999**, *99*, 355.
- (3) Tucker, S. C. *Chem. Rev.* **1999**, *99*, 391.
- (4) Tucker, S. C.; Maddox, M. W. *J. Phys. Chem. B* **1998**, *102*, 2437.
- (5) Brennecke, J. F.; Chateaufort, J. E. *Chem. Rev.* **1999**, *99*, 433.
- (6) Fernandez-Prini, R.; Japas, M. L. *Chem. Soc. Rev.* **1994**, 155.
- (7) Drozdov, A. N.; Tucker, S. J. *Phys. Chem. B* **2001**, *105*, 6675.
- (8) Maddox, M.; Goodyear, G.; Tucker, S. J. *Phys. Chem. B* **2000**, *104*, 6248.
- (9) Egorov, S. A.; Yethiraj, A.; Skinner, J. L. *Chem. Phys. Lett.* **2000**, *317*, 558.
- (10) Takebayashi, Y.; Kimura, Y.; Ohba, M. *J. Chem. Phys.* **2000**, *112*, 4662.
- (11) Yamaguchi, T.; Kimura, Y.; Hirota, N. *J. Chem. Phys.* **1999**, *111*, 4169.
- (12) Graf, P.; Nitzan, A. *Chem. Phys.* **1998**, *235*, 297.
- (13) Ganapathy, S.; Carlier, C.; Randolph, T. W.; O'Brien, J. A. *Ind. Eng. Chem. Res.* **1996**, *35*, 19.
- (14) Petsche, I. B.; Debenedetti, P. G. *J. Chem. Phys.* **1989**, *91*, 7075.
- (15) Siavosh-Haghighi, A.; Adams, J. E. *J. Phys. Chem. A* **2001**, *105*, 2680.
- (16) Heidelberg, C.; Vikhrenko, V. S.; Schwarzer, D.; Fedchenia, I. I.; Schroeder, J. *J. Chem. Phys.* **1999**, *111*, 8022.
- (17) Kitao, O.; Tanabe, K.; Ono, S.; Kumakura, S.; Nakanishi, K. *Fluid Phase Equilib.* **1998**, *144*, 279.
- (18) Patel, N.; Biswas, R.; Maroncelli, M. *J. Phys. Chem. B* **2002**, *106*, 7096.
- (19) Frankland, S. J. V.; Maroncelli, M. *J. Chem. Phys.* **1999**, *110*, 1687.
- (20) Song, W.; Biswas, R.; Maroncelli, M. *J. Phys. Chem. A* **2000**, *104*, 6924.
- (21) Patel, N.; Maroncelli, M. (in preparation).
- (22) Martin, M. G.; Siepmann, J. I. *J. Phys. Chem. B* **1998**, *102*, 2569.
- (23) Harris, J. G.; Yung, K. H. *J. Phys. Chem.* **1995**, *99*, 12021.
- (24) *Landolt-Bornstein, Numerical Data and Functional Relationships in Science and Technology*; Springer-Verlag: New York, 1974; Vol. II/6.
- (25) Penoncello, S.; Shan, Z.; Jacobsen, R. *ASHRAE Trans.* **2000**, *106*, 739.
- (26) Myers, D. J.; Shigeiwa, M.; Fayer, M. D.; Cherayil, B. J. *J. Phys. Chem. B* **2000**, *104*, 2402.
- (27) Biswas, R.; Lewis, J.; Maroncelli, M. *Chem. Phys. Lett.* **1999**, *310*, 485.
- (28) Kimura, Y.; Hirota, N. *J. Chem. Phys.* **1999**, *111*, 5474.
- (29) Rice, J. K.; Niemeyer, E. D.; Bright, F. V. *J. Phys. Chem.* **1996**, *100*, 8499.
- (30) Zhang, J.; Lee, L. L.; Brennecke, J. F. *J. Phys. Chem.* **1995**, *99*, 9268.
- (31) Akimoto, S.; Kajimoto, O. *Chem. Phys. Lett.* **1993**, *209*, 263.
- (32) Sun, Y.-P.; Fox, M. A.; Johnston, K. P. *J. Am. Chem. Soc.* **1992**, *114*, 1187.
- (33) Kajimoto, O.; Futakami, M.; Kobayashi, T.; Yamasaki, K. *J. Phys. Chem.* **1988**, *92*, 1347.
- (34) Saitow, K.; Ohtake, H.; Sarukura, N.; Nishikawa, K. *Chem. Phys. Lett.* **2001**, *341*, 86.
- (35) Neufeind, J.; Fischer, H.; Schroer, W. *J. Phys.: Condens. Matter* **2000**, *12*, 8765.
- (36) Nishikawa, K.; Morita, T. *Chem. Phys. Lett.* **2000**, *316*, 238.
- (37) Okazaki, S.; Terauchi, N.; Okada, I. *J. Mol. Liq.* **1995**, *65/66*, 309.
- (38) Okazaki, S.; Matsumoto, M.; Okada, I. *J. Chem. Phys.* **1995**, *103*, 8594.
- (39) Hloucha, M.; Deiters, U. *Fluid Phase Equilib.* **1998**, *149*, 41.
- (40) Potter, S.; Tildesley, D.; Burgess, A.; Rogers, S. *Mol. Phys.* **1997**, *92*, 825.
- (41) Lissal, M.; Vacek, V. *Fluid Phase Equilib.* **1996**, *118*, 61.
- (42) Palmer, B. J.; Anchell, J. L. *J. Phys. Chem.* **1995**, *99*, 12239.
- (43) van Leeuwen, M. E. *Fluid Phase Equilib.* **1994**, *99*, 1.
- (44) Gough, C.; DeBolt, S.; Kollman, P. J. *Comput. Chem.* **1992**, *13*, 963.
- (45) Bohm, H. J.; Ahlrichs, R.; Scharf, P.; Schiffer, H. *J. Chem. Phys.* **1984**, *81*, 1389.
- (46) One exception is the work of van Leeuwen<sup>43</sup> who fitted a Stockmayer potential to the coexistence curve of fluorofrom.
- (47) Panagiotopoulos, A. Z. *Mol. Phys.* **1987**, *61*, 813.
- (48) On the basis of work described in ref 20 we anticipated that the Lennard-Jones well depth  $\epsilon$  required to fit the coexistence properties would be roughly 10% larger than that the value of this parameter needed to best reproduce the experimental virial data.
- (49) Frenkel, D.; Smit, B. *Understanding Molecular Simulation*; Academic Press: New York, 1996.
- (50) Adams, D. J.; Dubey, G. S. *J. Comput. Phys.* **1987**, *72*, 156.
- (51) Allen, M. P.; Tildesley, D. J. *Computer Simulation of Liquids*; Oxford: Oxford, 1987.
- (52) Liu et al. already provided a parametrization of the diffusion constants of  $\text{CHF}_3$  using some of the same data used here. However, we found the parameters published in ref 59 to be inconsistent with the experimental data. We therefore refit the relevant portion of the data from ref 58. The fit yielded the model parameters  $\sigma_{\text{LJ}} = 3.874 \text{ \AA}$  and  $\epsilon_{\text{LJ}}/k_B = 336.0 \text{ K}$ .
- (53) Dymond, J.; Smith, E. *The Virial Coefficients of Pure Gases and Mixtures*; Clarendon Press: Oxford, 1980.
- (54) Rubio, R. G.; Zollweg, J. A.; Palanco, J. M. G.; Calado, J. C. G.; Miller, J.; Streett, W. B. *J. Chem. Eng. Data* **1991**, *36*, 171.
- (55) *Thermophysical Properties of Freons: Methane Series, Part 1*; Altunin, V. V., Geller, V., Petrov, E., Rasskazov, D., Spiridonov, G., Eds.; Hemisphere Publishing: Washington, DC, 1987.
- (56) Lewis, J.; Biswas, R.; Robinson, A.; Maroncelli, M. *J. Phys. Chem. B* **2001**, *105*, 3306.
- (57) Neumann, M. *Mol. Phys.* **1983**, *50*, 841.
- (58) Lang, E. W.; Prielmeier, F. X.; Radkowsky, H.; Ludemann, H.-D. *Ber. Bunsen.-Ges. Phys. Chem.* **1987**, *91*, 1025.
- (59) Liu, H.; Silva, C.; Macedo, E. *Chem. Eng. Sci.* **1998**, *53*, 2403.
- (60) Shan, Z.; Penoncello, S.; Jacobsen, R. *ASHRAE Trans.* **2000**, *106*, 757.
- (61) Neumann, M.; Steinhauser, O. *Chem. Phys. Lett.* **1983**, *102*, 508.
- (62) Bottcher, C. J. F.; Bordewijk, P. *Dielectrics in Time-Dependent Fields*; Elsevier: Amsterdam, 1978; Vol. II.
- (63) In calculating these spectra the experimental value of  $\eta_D^2$  was used for  $\epsilon_\infty$  and the simulated value of  $\epsilon_0$  was used for  $(\epsilon_0 - \epsilon_\infty)$ . The spectra are shown normalized because the data in ref 34 were presented in this manner.

The intensities do not contain information about the absolute intensity of the absorption. The absorption coefficients of the calculated spectra at their maxima are  $150\text{ cm}^{-1}$  at a density of  $0.13\ \rho_c$  and  $340\text{ cm}^{-1}$  at  $2.0\ \rho_c$ . On the basis of the intensities of the liquid-phase data of Gershel et al.<sup>66</sup> it seems likely that the experimental values are probably lower, due to the underestimation of the breadth of the spectra by the simulation model.

(64) Lisal, M.; Vacek, V. *Fluid Phase Equilib.* **1996**, *118*, 61.

(65) Bondi, A. *J. Phys. Chem.* **1964**, *68*, 441.

(66) Gershel, A.; Dimicoli, I.; Jaffre, J.; Riou, A. *Mol. Phys.* **1976**, *32*, 679.

(67) The structures depicted in Figure 1 and volume estimates are based on standard van der Waals radii<sup>65</sup> and the experimental equilibrium geometry<sup>24</sup> in the case of  $\text{CHF}_3$  ( $V = 42\ \text{\AA}^3$ ) and Lennard-Jones diameters in the case of the simulation model ( $V = 37\ \text{\AA}^3$ ).